Spectral flow cytometry for detecting DNA cargo in malaria parasite–derived extracellular vesicles

Received for publication, December 12, 2024, and in revised form, March 11, 2025 Published, Papers in Press, April 6, 2025,
https://doi.org/10.1016/j.jbc.2025.108481

Ewa Kozela[1], Ekaterina Petrovich-Kopitman[2], Yuval Berger[1], Abel Cruz Camacho[1], Yaara Shoham[1], Mattia I. Morandi[3,4], Irit Rosenhek-Goldian[5], Ron Rotkopf[6], and Neta Regev-Rudzki[1,*]

From the [1]Department of Biomolecular Sciences, Faculty of Biochemistry, Weizmann Institute of Science, Rehovot, Israel; [2]Flow Cytometry Unit, Life Sciences Core Facilities, Weizmann Institute of Science, Rehovot, Israel; [3]Institute of Organic Chemistry and Biochemistry of the Czech Academy of Science, Prague, Czech Republic; [4]The International Institute of Molecular Mechanisms and Machines, Polish Academy of Sciences, Warsaw, Poland; [5]Department of Chemical Research Support, Weizmann Institute of Science, Rehovot, Israel; [6]Bioinformatics Unit, Life Science Core Facilities, Weizmann Institute of Science, Rehovot, Israel

Reviewed by members of the JBC Editorial Board. Edited by Ronald Wek

Cells across biological kingdoms release extracellular vesicles (EVs) as a means of communication with other cells, be their friends or foes. This is indeed true for the intracellular malaria parasite *Plasmodium falciparum* (*Pf*), which utilizes EVs to transport bioactive molecules to various human host systems. Yet, the study of this mode of communication in malaria research is currently constrained due to limitations in high-resolution tools and the absence of commercial antibodies. Here, we demonstrate the power of an advanced spectral flow cytometry approach to robustly detect secreted EVs, isolated from *Pf*-infected red blood cells. By labeling both EV membrane lipids and the DNA cargo within (non-antibody staining approach), we were able to detect a subpopulation of parasitic-derived EVs enriched in DNA. Furthermore, we could quantitatively measure the DNA-carrying EVs isolated from two distinct blood stages of the parasite: rings and trophozoites. Our findings showcase the potential of spectral flow cytometry to monitor dynamic changes in nucleic acid cargo within pathogenic EVs.

Extracellular vesicles (EVs) are membrane-bound organelles (∼50–500 nm) released by living cells across kingdoms (1, 2). EVs serve as a powerful cell–cell communication mechanism as they shuttle diverse cargo components between cells (3). These secreted vesicles mediate interspecies host–pathogen communication (4–6), including parasitic infections (7–15).

Human parasitic diseases, such as malaria (caused by *Plasmodium* parasites), leishmaniasis (*Leishmania*), or Chagas disease (*Trypanosoma*), affect millions of people yearly and have enormous health and economic impact worldwide (14), (https://www.who.int/teams/global-malaria-programme/reports/world-malaria-report-2023, https://www.who.int/health-topics/neglected-tropical-diseases#tab=tab_1). EV concentration and content change in response to distinct physiological and pathological conditions (16), closely reflecting the cell or disease states (14, 17, 18). EV-based screening for disease diagnosis has been proposed as an exciting opportunity to develop early, noninvasive prediction tools (19–21). One of the major challenges in EV research, however, is the absence of efficient, quantitative, high-throughput tools for studying vesicle heterogeneity, primarily due to the nanoscale size of EVs and the limitations of current technologies (22–24).

Malaria remains the most severe parasitic disease worldwide, with nearly 200 million disease cases and ∼600,000 deaths annually (https://www.who.int/teams/global-malaria-programme/reports/world-malaria-report-2023), (25, 26). The disease is transmitted by the intracellular parasite *Plasmodium*, with the *Plasmodium falciparum* (*Pf*) species responsible for the most severe malaria cases (27). *Pf* parasites circle between *Anopheles* mosquitoes and humans, where they reside and multiply inside the host red blood cells (RBCs) (25, 28). EVs secreted by malaria parasite are crucial mediators of parasite invasion, growth, immunomodulation, and even host-vector transmission (15, 29–35). *Pf* EVs are efficient carriers of coding and noncoding RNAs which activate monocytes (36–38), NK cells (39), and modify host immune responses for the benefit of the parasite survival (37). Fascinatingly, *Pf* EVs also shuttle DNA cargo (35), activating host DNA cellular sensors and gene expression (40). Severe cases of human *Pf* infections are correlated with highly elevated plasma EVs levels (41–43) and are declined in response to the malaria treatment (44), pointing to the promising possibility of establishing *Pf* EV titers as a diagnostic tool.

Generally, EVs are composed of subpopulations which are heterogeneous in their nano-sizes, cargo, biophysical properties, and cellular destinations (9, 22, 29, 45–47). Current EV characterization is mainly size-driven and based on imaging approaches to include nanoparticle tracking analysis (NTA (48)), asymmetric field flow fractionation (AF-4) (29, 49), atomic force microscopy (AFM) (29, 50), and cryo-transmission electron microscopy (cryo-TEM (51)). However, these analytical methods do not distinguish between EV subclasses defined by EV specific markers, including EV-cargo components. Multiple efforts have been employed to develop

* For correspondence: Neta Regev-Rudzki, neta.regev-rudzki@weizmann.ac.il.

nano-scaled techniques that can detect EV subpopulations (24, 52). Classifying EVs based on their cargo is particularly challenging in the case of malaria (53). This is due to the lack of commercially available antibodies against malaria parasite, imposing the use of generic dyes labeling EVs and/or EV cargo components (36, 38, 53).

In this study, we utilized the advanced spectral flow cytometry apparatus (54, 55) to demonstrate not only the detection of EVs released from *Pf*-infected RBCs (*Pf* EVs) but also the ability to specifically track their DNA cargo. We were able to double-label the EVs based on their membrane lipid components and DNA cargo and demonstrate that a subpopulation of the secreted EVs is enriched with DNA. Moreover, using this approach, we demonstrated that the DNA cargo enrichment is specific to EVs secreted by the early ring-stage of the parasite, in contrast to EVs secreted during the late trophozoite stage of malaria infection. Together, these results indicate that the spectral flow cytometry approach could be applied for monitoring EV subpopulations, based on their nucleic cargo.

Results

Detection of Pf*-derived EVs using spectral flow cytometry*

We aimed to determine whether EVs harvested from *Pf*-infected RBCs (*Pf* EVs) and uninfected naïve RBCs (Ui EVs) could be detected using the advanced Cytek Aurora spectral flow cytometry system. EV isolation (29) was initially validated using three independent approaches, NTA measurement, cryo-TEM, and AFM imaging (Fig. 1). NTA analysis showed that the isolated *Pf* EVs were within the expected size range of 80 to 160 nm, with a peak of ∼100 nm population (Fig. 1*A*). We then employed OptiPrep density gradient (51) for the EV samples and imaged them by cryo-TEM (51) to confirm the bilayer membrane EV structure and size (Fig. 1*B*). Finally, *Pf* EVs purified *via* sucrose cushion (50) were imaged using AFM (Fig. 1*C*), which demonstrated round structures with sizes consistent with the NTA and cryo-TEM analyses.

Having validated the *Pf* EV characteristics, we proceeded to examine whether the isolated EVs, despite their nano-sizes could be detected using spectral flow cytometry. In the initial approach, we applied the scatter light analysis of the unstained samples in an effort to estimate the relative EV size (diameters) as well as to differentiate the EVs from the control PBS sample (background) (56, 57). However, we observed no difference in the side scatter (SSC) and forward scatter (FSC) features between the PBS, Ui EV, and *Pf* EV samples (Fig. S1*A*). Increasing the gain of SSC detector to very high value, although caused improvement in EVs detection above noise, still did not succeed in detecting smallest EVs that remained in the noise region (Fig. S4). Therefore, EV samples could not be differentiated (gated out) based exclusively on their light scatter characteristics.

Since the light scatter analysis did not allow clear separation of the EV sample from PBS and the instrument background, we proceeded to analyze the EV samples based on their fluorescent emission parameters. To address this, we stained the membranes of the parasitic EVs using the lipophilic pan-EV dye R18 (58). The advantage of the R18 dye is that it belongs to the rhodamine family of dyes which were described to be photostable and highly fluorescent, enabling staining at low dye concentrations (58, 59). R18 exhibits self-quenching properties when present at high, free dye concentrations, while turning bright fluorescent upon dilution, that is, binding with membranes *via* membrane lipid moieties (58, 59). We first estimated the labeling efficiency based on the fluorescent signal received from stained *Pf* EV compared to unstained EVs, serving as a control. We recorded and compared the spectral signatures of *Pf* EV samples, which were either unstained or labeled with R18 pan-EV lipid dye. We detected significant fluorescent signal in the R18-stained *Pf* EVs, clearly distinct from unstained *Pf* EVs (Fig. 2*A*). The peak emission area registered in R18 was within yellow green (YG) detection channels and with YG1 as peak channel (wavelengths 567–587, Fig. 2*A*), corresponding to the known emission fluorescence ranges of R18 (58). We used the unstained control samples to set the gating of the measurement (Fig. 2*B*). Some background of R18+ signal was detected in the samples derived from the control of cell-free media (Fig. S1*C*). We assumed that the lipophilic R18 dye binds also lipoproteins present in the lipid-rich albumin-supplemented *Pf* media, contributing to the signal background as previously reported (60, 61).

Upon confirming the ability to detect R18-labeled EVs using the spectral flow cytometer, we proceeded to measure the R18 labeling efficiency of EVs derived from different samples, including those from control uninfected (Ui) RBCs and *Pf*-infected RBC cultures (Fig. 3*A*).

Equal concentrations of EVs (Fig. 3*B*) were loaded into the spectral flow cytometer, and the efficiency of R18 labeling for Ui and *Pf* EV samples was determined (Fig. 3*C*). We found a similar level of R18+ signal for Ui and *Pf* EV samples (Fig. 3*C*). These data confirmed that indeed the labeling by the R18 lipid dye is equally efficient for both types of EVs (Ui and *Pf* EVs). The use of flow cytometry for EV analysis is known to hold the risk of swarm detection, where multiple nanoparticles may be detected as a single event due to the instrument's detection limits, potentially resulting in inaccurate particle concentration measurements (62). To exclude the probability of a swarm effect during data acquisition (56), we screened serial dilutions of R18-stained *Pf* EVs. The serial dilution approach showed that the number of detected R18-labeled EVs decreased proportionally to the sample dilution factor while the R18-specific peak fluorescence intensity (YG1-H) did not change across subsequently diluted R18+ EV samples, indicating that the data acquisition is performed within the proper EV concentration ranges (Fig. S1*E*) and the measurements can be performed at a wide range of R18-EV concentrations (Fig. S3). Labeling the EVs by the R18 resulted in a change in their scatter light signal (SSC-H/FSC-H), with the SSC-H/FSC-H profile of the R18-labeled EVs extended beyond the signal observed in the unstained EVs sample (Fig. S1*B* *vs* Fig. S1*A*).

As a complementary approach, to validate the data obtained with R18-stained EVs, we stained the *Pf* EVs with an additional

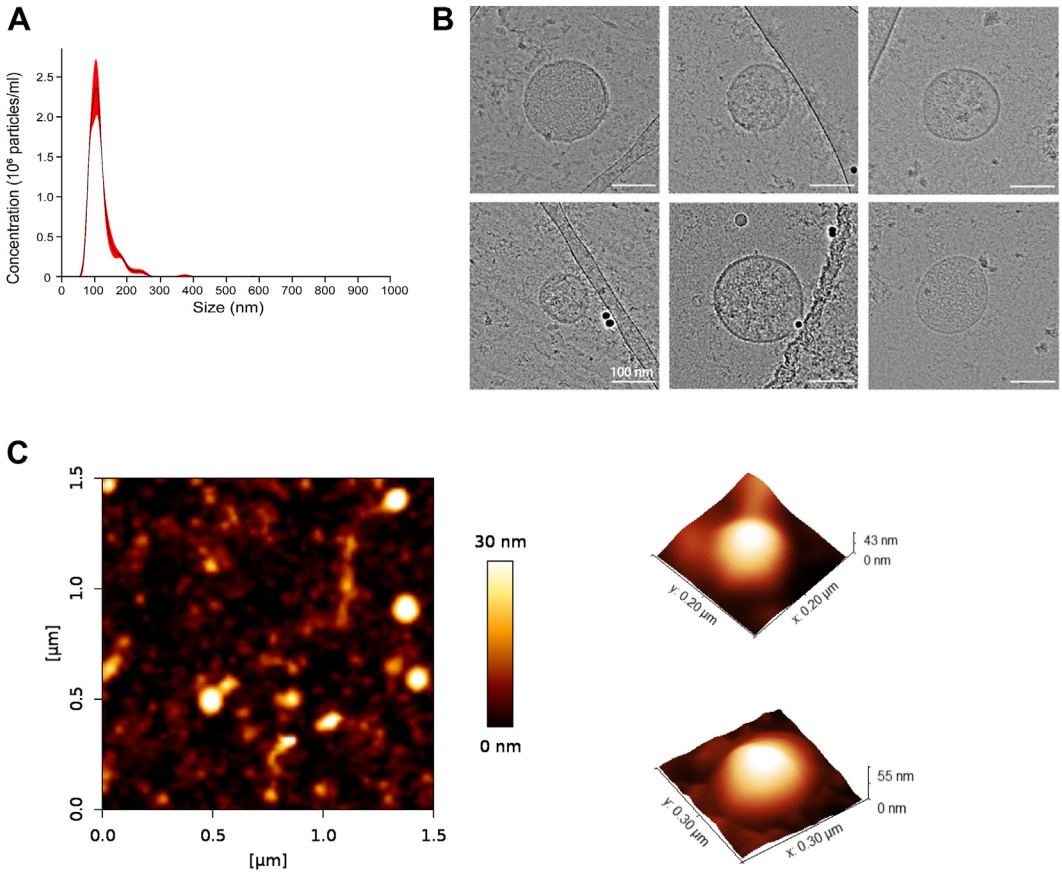

Figure 1. Size, concentration, and morphology characterization for EVs derived from *Pf* iRBCs. *A*, nanoparticle tracking analysis (NTA) measurement of *Pf* EV concentration and size distribution. *B*, representative cryo-transmission electron microscopy (cryo-TEM) images of isolated *Pf* EVs, with visible lipid bilayer and size in agreement with measured diameter distribution by NTA (scale bar represents 100 nm). *C*, atomic force microscopy (AFM) image of *Pf* EVs adsorbed on Mg^{2+}-modified mica, along with representative 3D AFM images of single *Pf* EVs.

membrane-labeling dye, ExoBrite CTB 560. ExoBrite CTB 560 is a fluorescent conjugate of cholera toxin subunit B (CTB), which binds to GM1 gangliosides, commonly found on the surface of cells, lipid rafts, and EVs (63, 64). ExoBrite CTB 560 possesses fluorescence spectra similar to R18 (excitation/emission 560/585) (58).

First, we tested whether the *Pf* EVs labeled with ExoBrite 560 lipid dye could be detected using the spectral flow cytometer. Indeed, following staining of *Pf* EVs with ExoBrite 560, we recorded the spectral signature of ExoBrite 560-labeled *Pf* EVs which exposed selective fluorescent emission within YG detectors and with peak YG1 channel (Fig. 2*A*), corresponding to the defined emission spectra of this lipid dye. In search for total ExoBrite 560-labeled EVs populations, we applied a gating strategy similar to the one described for R18-labeled EVs where we compared lipid dye–labeled EVs to the unstained samples. This way, we defined total pools of ExoBrite 560-labeled EVs in Ui and *Pf* EV samples (Fig. 2*C*) to be referred to in further analysis. The comparison of unstained and ExoBrite 560-stained EVs revealed populations of ExoBrite 560-positive Ui EVs and *Pf* EVs (Figs. 2*C* and 4*A*). However, we detected approximately 5 to 10% ExoBrite 560-labeled EVs (out of all EVs loaded) (Fig. 4*B*), indicating a much lower labeling efficiency of this dye as compared to the R18 dye (Fig. 2*B*). Negligible fluorescent signal was detected in the control, lipid dye–only samples (non EVs). Notably, the control R18-stained PBS sample (Fig. S1*C*) and the ExoBrite 560-stained PBS sample (Fig. S2*A*) exhibited very low fluorescent signals, confirming that free lipid dyes are efficiently cleared from the samples.

In summary, these results demonstrate that spectral flow cytometry enables the detection of lipid-labeled EVs with efficient labeling.

Detection of parasitic EV-DNA cargo using spectral flow cytometry

Previously it was shown that *Pf* EVs contain *Pf* genomic DNA (35, 40, 53, 65). In order to examine whether the DNA cargo within *Pf* EVs could be detected by the spectral flow cytometry, we used the DNA dye DRAQ5 (66), which was shown to label EV-DNA (67). EVs harvested from uninfected RBCs (Ui RBCs) were used as control, since they are lacking DNA cargo (40).

First, we tested if it is possible to detect fluorescence signal for *Pf* EV which were stained with the DRAQ5 dye. Indeed, DRAQ5-stained *Pf* EV samples exhibited distinct fluorescent

Spectral flow cytometry for EV and cargo detection

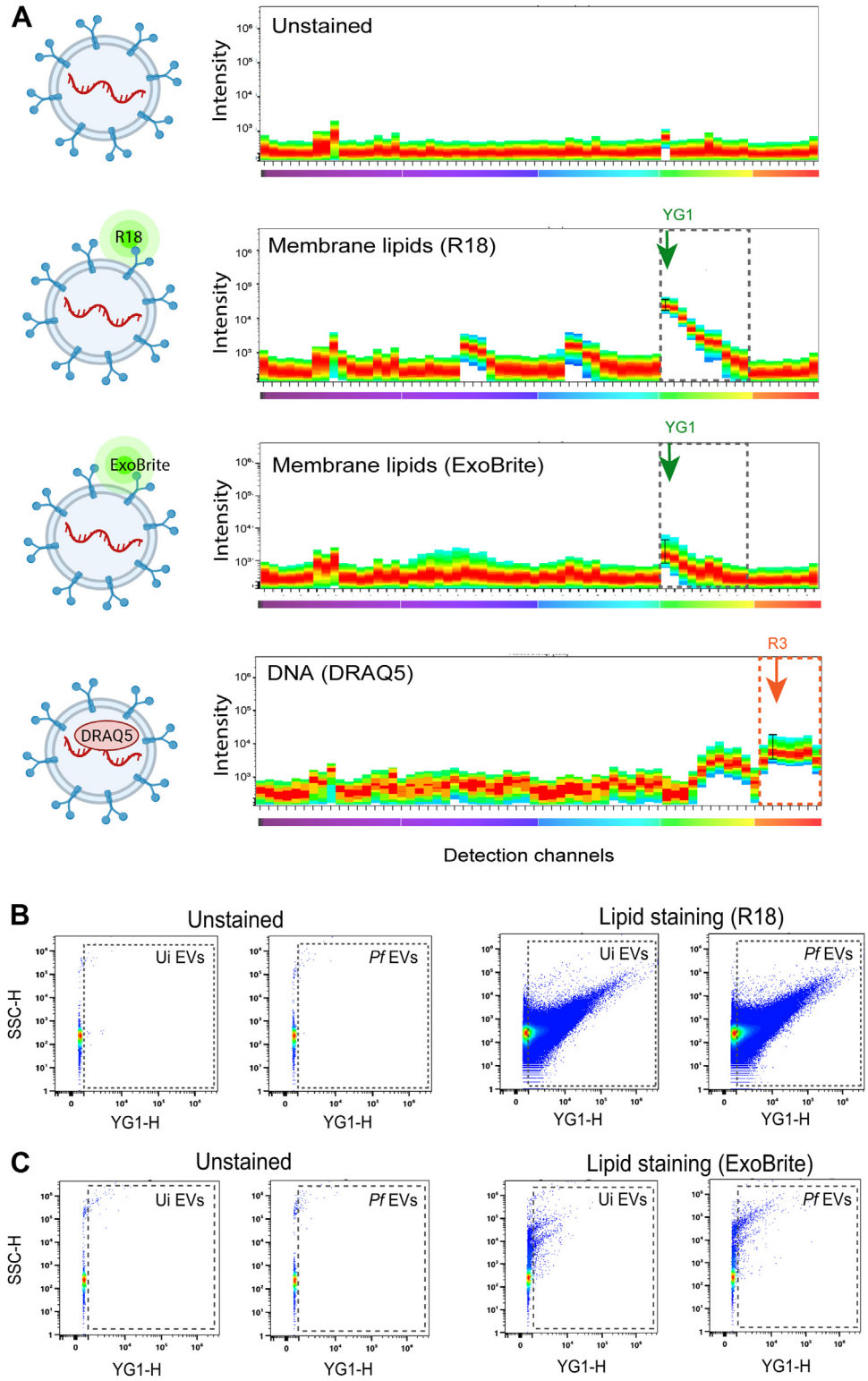

Figure 2. Detection of parasitic *Pf* EVs using spectral flow cytometry. *A*, representative spectral flow cytometry diagrams (signatures) for unstained *Pf* EVs, *Pf* EVs labeled with membrane lipophilic dyes (R18, ExoBrite 560), and with DNA dye (DRAQ5), all single dye–stained samples. Dashed areas indicate main fluorescent areas with peak *yellow green* 1 (YG1, *green* arrow) detection channel in R18- and ExoBrite 560-labeled samples (for EV membranes) and peak *red* channel (R3, *red* arrow) for DRAQ5-labeled samples (EV DNA cargo). *B* and *C*, representative pseudo-color flow cytometry plots of (*B*) unstained EVs, EVs labeled by R18 derived from control uninfected RBCs (Ui) and *Pf* EVs (n = 3), and (*C*) unstained EVs and ExoBrite 560-labeled Ui and *Pf* EVs (n = 3); *dashed* areas indicate R18+ or ExoBrite 560+ labeled EVs gated within peak YG1 detection channel (YG1-H). SSC-H, side scatter height.

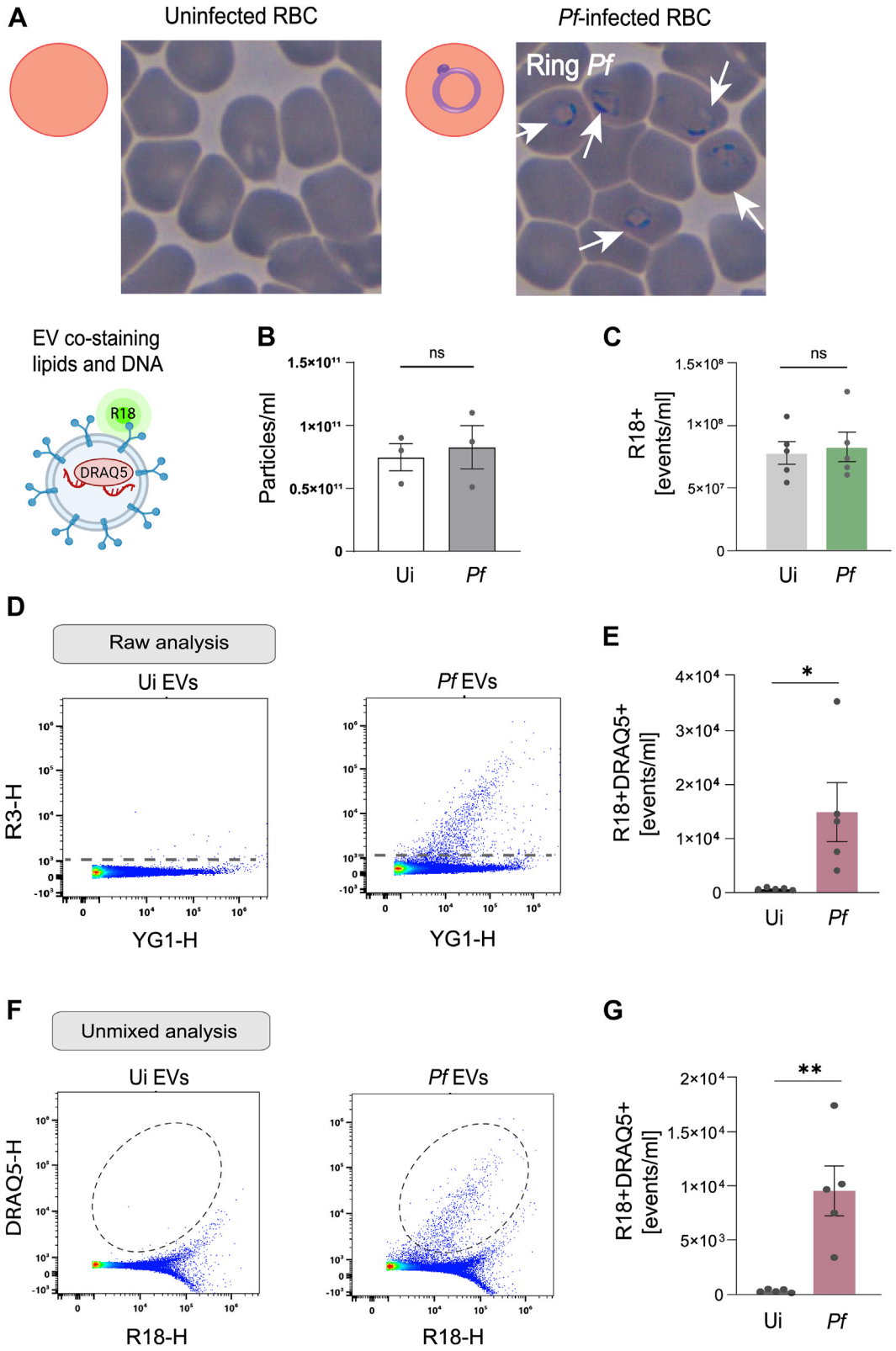

Figure 3. Spectral flow cytometry detection of *Pf* iRBC-derived EVs enriched with DNA cargo. *A*, Giemsa staining of uninfected RBCs (Ui) and ring-stage *Pf* iRBCs (*white* arrows). *B*, NTA-analysis of EVs isolated from uninfected RBCs (Ui EVs) and from ring-stage *Pf* iRBCs (*Pf* EVs, (n = 3). *C*, average concentrations of EVs derived from Ui and ring stage *Pf* RBCs labeled with R18 lipid dye (R18+) using spectral flow cytometry measurement (n = 5). *D*, representative flow cytometry dot plots showing concentrations of EVs co-labeled with R18 (membrane lipids) and DRAQ5 (DNA cargo) dyes within total R18+ EV populations derived from Ui RBCs and from *Pf* iRBCs (Ui EV and *Pf* EVs, respectively), raw data analysis approach. *E*, the averaged ± SEM concentrations of Ui and *Pf* EVs detected as double stained R18+DRAQ5+; the data are presented as bar graphs obtained using raw data approach (n = 5). *F* and *G*, the results of unmixing analysis, including (*F*) representative dot plots derived from spectral flow cytometry analysis of Ui EV and *Pf* EVs and (*G*) averaged concentrations ± SEM of Ui EVs and *Pf* EVs detected as double positive R18+DRAQ5+ (n = 5). Symbols: *$p < 0.05$, **$p < 0.01$, ns – nonsignificant (unpaired t tests). YG1-H, *yellow green* 1 main detection channel for R18 labeling lipid membranes, R3-H, red channel 3 for DRAQ5 as of DNA labeling.

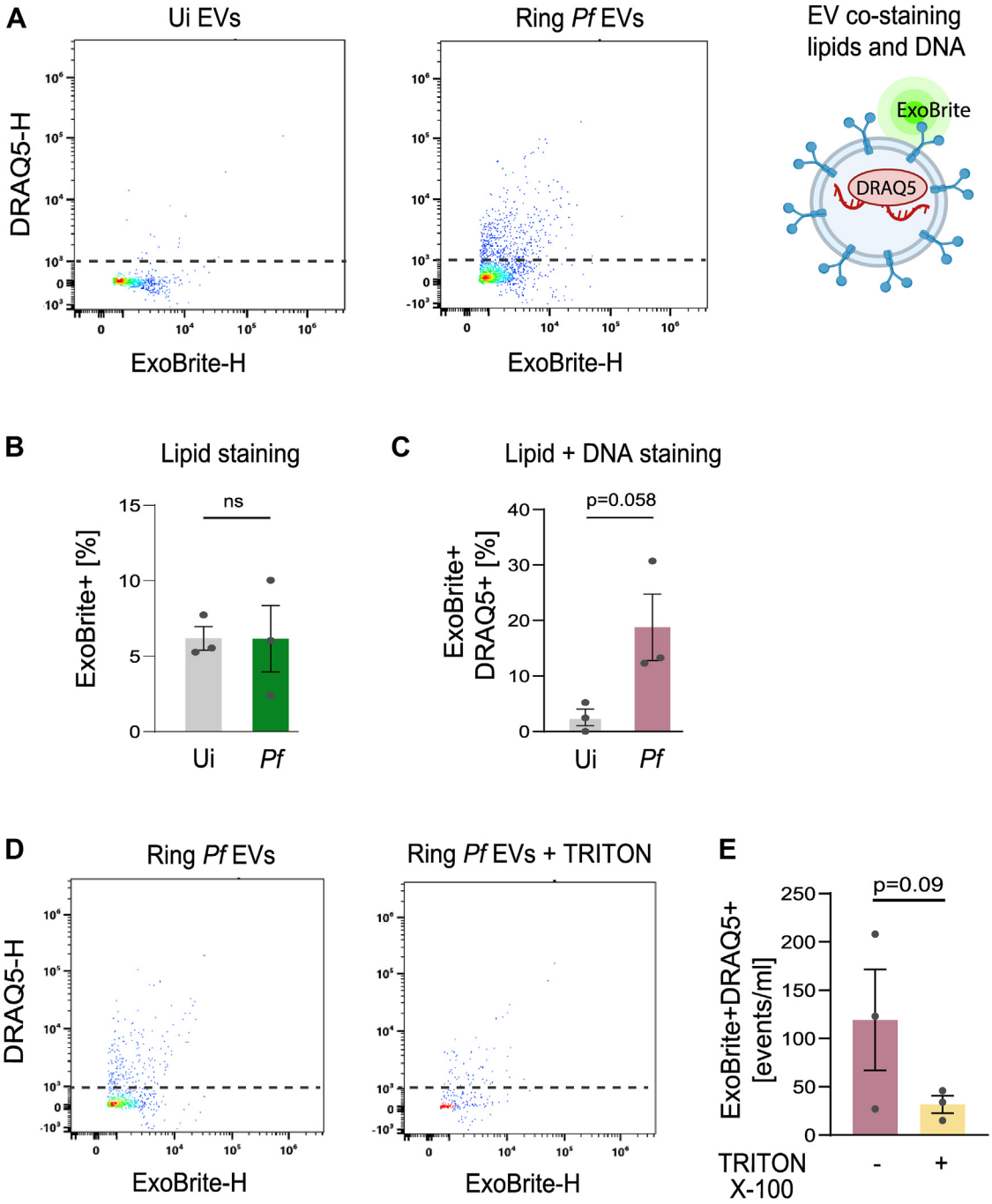

Figure 4. Detection of DNA cargo in *Pf* EVs. *A*, representative dot plot diagrams of Ui and *Pf* EVs costained with the membrane lipid dye (ExoBrite 560) and a DNA dye (DRAQ5). *B*, average ± SEM percentages of EVs derived from Ui RBCs and *Pf*-iRBCs positive for ExoBrite 560 signal within total loaded EVs (equal to 100% in each experiment) detected by spectral flow cytometry. *C*, average ± SEM percentages of *Pf* EVs and control Ui EVs double positive for ExoBrite 560 (lipid membrane) and DRAQ5 (DNA; n = 3, *p* values of unpaired *t* test). *D* and *E*, the effects of detergent treatment (TRITON X-100) on double stained *Pf* EVs (ExoBrite560+DRAQ5+), including (*D*) dot plot representatives and (*E*) the average *Pf* EV concentrations ± SEM, double labeled with ExoBrite 560 and DRAQ5, before and after the detergent treatment (n = 3, paired *t* test).

signature with clear emission intensity within red detection channels (R) and R3 peak channel (688–707 nm; Fig. 2*A*), corresponding to the known emission fluorescence range of DRAQ5 (66). These data indicated that DNA cargo can be labeled using spectral flow cytometry.

Since the labeling efficiency of R18-labeled EVs is similar for EVs derived from *Pf*-infected RBCs (*Pf*-iRBCs) and control Ui RBCs samples (Fig. 3*C*), we proceeded to compare the levels of DNA cargo signal associated with the membrane labeled EVs. Isolated EVs from both samples were costained with the DNA dye (DRAQ5) combined with the R18 membrane-lipid dye to ensure detecting membrane-bound DNA. The spectral flow cytometry apparatus offers two data analysis approaches, (a) raw analysis, which is based on the comparison of raw fluorescence intensity from peak (or other selected) detection channels, as well as (b) analysis *via*

unmixing algorithm, with or without autofluorescence deduction, which is software driven, unbiased comparison of overlayed spectral signatures recorded from individual samples (54, 55). We thus initially analyzed the EV samples using raw intensities from peak dye emission channels, that is, YG1 channel for R18 and R3 channel for DRAQ5 signal. This analysis revealed that Ui EVs are devoid of costained R18+DRAQ5+ EVs, indicating the lack of DNA cargo in the EVs derived from uninfected RBCs (Fig. 3, *D* and *E*). Remarkably, the *Pf* EVs sample showed significantly higher signal intensity for the double-labeled R18+DRAQ5+, demonstrating the presence of parasitic EVs encapsulating DNA (Fig. 3, *D* and *E*). Applying the unmixing algorithm onto these raw fluorescent intensity data further confirmed the profound difference between the parasitic EVs and the control Ui EVs (Fig. 3, *F* and *G*).

We next confirmed that the combined R18- and DRAQ5-labeling does not lead to cross-dye interference, that is, fluorescent signal leakage of one dye into the detection peak channels of the other dye(s). To address that, we performed a series of control measurements using single stained EV samples. The spectral flow cytometry analysis of unstained *Pf* EVs showed no fluorescent emission within the R3 channel, indicating the absence of autofluorescence in the DNA dye-specific channels. Subsequent analysis of the R18-only–stained *Pf* EV sample showed no leakage of R18 emission into the DRAQ5-specific R3 detection channel. Moreover, we observed no leakage of DRAQ5 emission into R18-specific YG1 channel (Fig. S1*D*). No DRAQ5+ events were detected in control cell-free cRPMI sample (Fig. S1*D*). These results confirmed a clear separation of dye-specific fluorescent signals for the Ui and *Pf* EV samples, with no nonspecific DNA-like signal detected in the control samples, supporting the reliability of this dye combination for detecting EV-encapsulated DNA. Moreover, additional validation of EV double labeling was supported by *in silico* comparison of the R18 and DRAQ5 spectras (Fig. S1*F*) as well as of the ExoBrite 560 and DRAQ5 spectras (Fig. S2*B*).

Unmixing analysis performed on the ExoBrite 560- and DRAQ5-double labeled samples revealed an increase in the DNA signal associated with *Pf* EVs in comparison to control Ui EVs (Fig. 4*C*). Importantly, detergent treatment caused a profound disruption of the fluorescent particles (Fig. 4, *D* and *E*), indicating that the detected DNA is encapsulated within lipid-labeled EV membranes. These data further support the results obtained using R18- and DRAQ-labeled EVs.

Together, these data demonstrate that the spectral flow cytometry apparatus can robustly detect both EVs and their DNA cargo.

Profiling Pf *EV subpopulations based on their DNA cargo levels using spectral flow cytometry*

Previously it was shown that *Pf* genomic DNA is present within *Pf* EVs that were secreted from the early blood stage (ring) of the parasite but absent (or cannot be detected) in EVs produced at the later blood stage (trophozoite) (40, 53). We thus examined whether the spectral flow cytometry approach is a sensitive method that enables the detection of distinct EV subpopulations differing in their DNA levels.

To assess this, we isolated EVs from *Pf* ring-stage–infected RBCs (approximately 10 h post invasion of the parasite into the host RBCs) and from the trophozoite *Pf* blood-stage (approximately 24 h post invasion of the parasite into the host RBCs) (Fig. 5*A*). The isolated EVs were stained for their lipid-membrane (R18) and the DNA cargo (DRAQ5), followed by spectral flow cytometry analysis (Fig. 5). In line with previous studies, we show a significantly higher DNA fluorescent signal in EVs derived from ring-stage *Pf*-iRBCs compared to those harvested from the trophozoite stage (Fig. 5, *B–D*). Importantly, the concentrations of total R18-labeled EVs did not differ between the different types of EVs, excluding the possibility that the observed difference in the DNA fluorescent signal stems from differences in total counts of the vesicles (Fig. 5*C*).

To confirm that the fluorescent signal is from the double-labeled EVs (R18+DRAQ5+), we treated the samples with a Triton X-100 detergent (68). The detergent treatment led to a significant decrease in R18+ and R18+DRAQ5+ EVs (Fig. 5, *E–G*), confirming that the DNA signal results from the cargo encapsulated within the EVs.

Collectively, these findings indicate that the spectral flow cytometry not only facilitates the quantification of rare EV subpopulations encapsulating parasitic DNA but also allows tracking dynamic changes in EV-DNA content across various parasite blood stages.

Discussion

In the present study, we demonstrate that the spectral flow cytometry apparatus could be used as a reliable tool for the detection of *Pf* EVs. Moreover, it allows identification of rare subpopulations of *Pf* EVs carrying DNA cargo. Our optimized approach using the cytometer allowed (a) detecting and quantifying concentrations of DNA-enriched EVs within total EV pools, (b) tracking changes in DNA-EV levels along parasite growth stages, and (c) differentiation of molecule complexes from free molecules or dyes based on response to detergent treatment (68).

For numerous systems, EV cargo detection has been limited due to the significant methodological challenges associated with its labeling. For example, permeabilizing EVs to allow antibody access is challenging without compromising their integrity. Omics profiling of bulk EV samples remains by far the main approach for cargo characterization, but it demands sample lysis and disregards EV subclasses (29, 52, 69). Consequently, current EV cargo analysis relies on antibody-based surface labeling and includes techniques such as microscopy, nanoscopy, and standard flow cytometry (24, 52, 69). Laborious bioengineering techniques in *in vitro* and *in vivo* models have been engaged to introduce optical reporters for EV cargo components to visualize cargo loading, transfer, and effector function in the recipient cells (70). Nanoscopies, including several super resolution techniques, open an exciting possibility for a thorough EV characterization; however, they lack high-throughput and multiparametric analytical capabilities (24, 56, 57, 71–77).

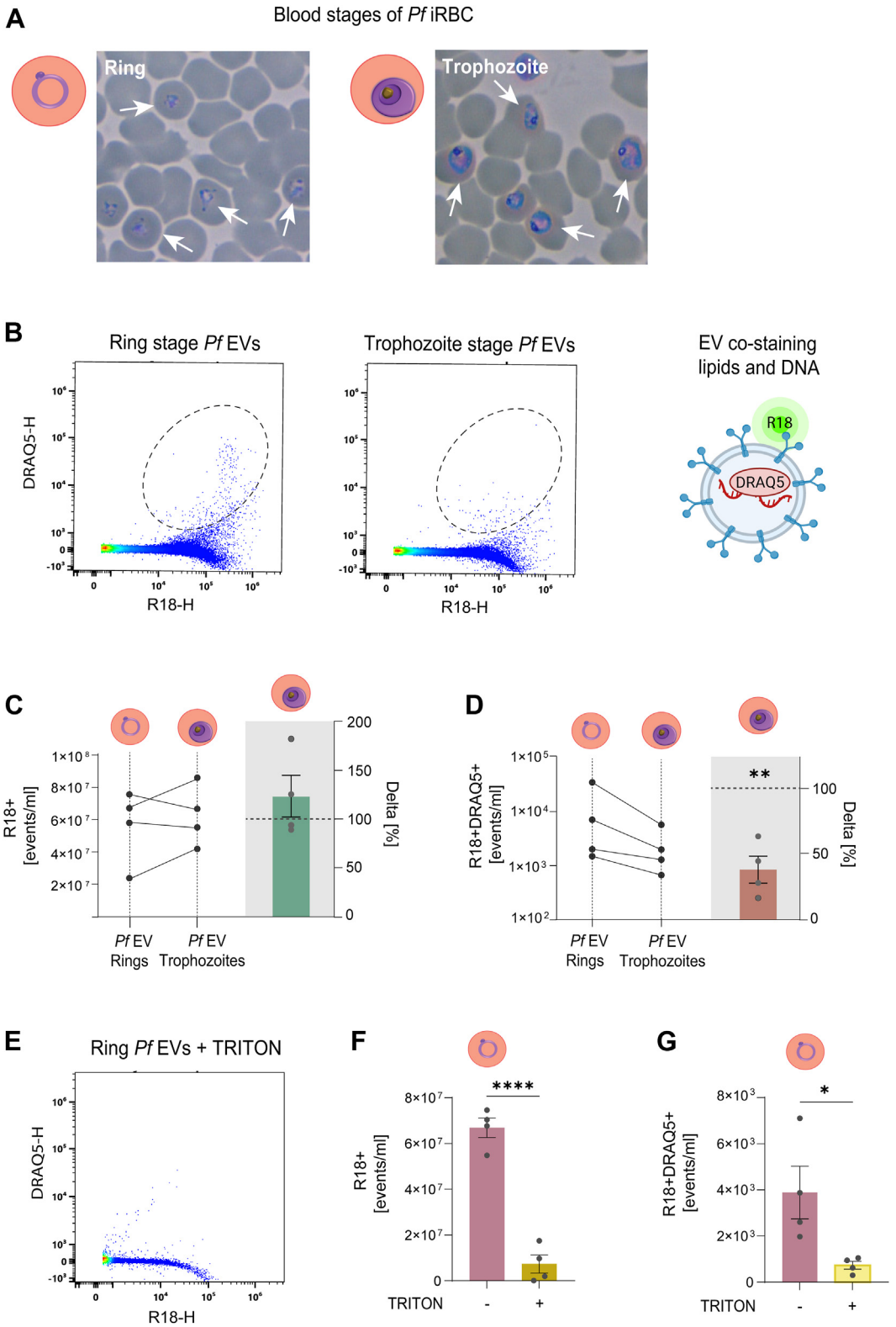

Figure 5. Spectral flow cytometry analysis for DNA cargo for *Pf* EVs derived from the ring-stage and trophozoite-stage *Pf*-iRBCs. *A*, Giemsa staining of *Pf*-iRBCs from the ring and trophozoite blood stages (*white* arrows). *B*, representative flow cytometry dot plot graphs for *Pf* EVs derived from either ring stage or trophozoite blood *Pf* stage labeled with R18 (membrane lipid) and DRAQ5 (DNA cargo). *C*, comparison of the concentrations of *Pf* EVs positive for lipid labeling (R18+) derived from ring stage and trophozoite stage *Pf*-iRBCs with each dot-pairing line representing a separate experiment (n = 4); adjacent *green* bar represents an averaged percentages of change in *Pf* EV concentrations labeled with lipid dye (R18+) between the two parasitic blood stages (delta [%], when ring stage *Pf* EV-R18+ levels equals to 100% in each experiment). *D*, concentrations of *Pf* EVs double positive for lipid membrane and DNA signal (R18+DRAQ5+) derived from ring or trophozoite *Pf* blood stages and the percentage change between the two *Pf* blood stages (n = 4, paired *t* test). *E*, representative dot plot graphs *Pf* EVs double positive for lipid membrane and DNA signal (R18+DRAQ5+) derived from ring-stage *Pf*-iRBCs treated with TRITON X-100. *F*, averaged concentrations of ring-stage *Pf* EVs detected as R18+ (lipid labeling) and (*G*) double positive for lipid and DNA labeling (R18+DRAQ5+), before and after TRITON X-100 treatment (n = 3, paired t tests). Symbols: *$p < 0.05$, **$p < 0.01$, ****$p < 0.0001$.

Characterization of EVs by flow cytometry is highly challenging (72), with collaborating efforts to standardize and improve reporting (MIFlowCyt-EV (56)). Most current flow cytometry instruments (a) have insufficient sensitivity to detect nanoscale EVs using light scatter signals, (b) lack the sensitivity to detect weak EV-bound fluorophore levels, and (c) suffer from overlapping instrument (optics, electronics) and sample (biological components, buffers, vehicles) noise, which complicates the interpretation of the results (72, 78, 79). Moreover, the application of the synthetic beads for EV size estimation has been recently questioned. This is due to the significantly different refractive indexes of the synthetic and cell-derived nanoparticles, consequently misrepresentation of cell-derived EVs by beads while using scatter light characteristics for particle size assessment (80–83).

The two lipophilic probes used in this study (R18 and ExoBrite 560) exhibit distinct labeling patterns and varied in the fluorescent intensity, with robust R18 staining as compared to the ExoBrite 560 signal. These differences may be due to the following: (a) dyes bind different lipid moieties on EV membranes, either abundant or low-moderately present, (b) fluorophores have different strengths, stabilities, and resilience to the processing required by the protocol (post staining EV purification, ultracentrifuging, light exposure), and (c) efficiency of ExoBrite 560 may vary, depending on EV source cells.

Other applications of spectral flow cytometry for EV analysis include phenotyping clinical samples of EVs isolated from serum, for instance, in the case of glioblastoma patients (84), using surface markers. Our results show that this robust method enables tracking of cargo components, present at very low concentrations within rare EV subpopulations. The lack of commercially available antibodies against malaria parasite imposes the use of dyes (58, 59, 85) for labeling *Pf* EVs and the different cargo components (36, 38, 53).

It is important to note that one of the limitations of using generic dyes is the need to define the limits of detection using the described method. In order to define the limit of fluorescence detection, Molecules of Equivalent Soluble Fluorophore (MESF) beads are often used (86). Calibration using MESF beads relies on comparing the fluorescence intensity of the sample to a set of beads with a known number of fluorophores. This enables the estimation of the absolute number of dye molecules on EVs (86). However, MESF beads are not available for fluorescent dyes such as R18 or DRAQ5. Consequently, it is challenging to determine the levels of R18 or DRAQ5 in absolute units and define limit of detection in absolute units.

The development of high throughput assays based on these dyes may fundamentally advance our understanding of malaria EV biology, enabling identifying parasitic EV subpopulations and their biological effects on diverse host cells, ultimately paving the way to malaria treatment and/or prevention.

Experimental procedures

P. falciparum *parasite line*

P. falciparum (*Pf*) malaria parasite line NF54 was used in this study. *Pf* NF54 was generously provided by the Malaria Research Reference Reagent Resource Center, MR4, obtained through BEI Resources, NIAID, NIH: *P. falciparum*, strain NF54 (Patient Line E), MRA-1000, contributed by Megan G. Dowler.

Pf *parasite culture*

Pf parasites were cultured in human RBCs using an established method (87). The parasites were grown in 4% hematocrit in pooled healthy Ui RBCs, provided by the Israeli blood banks (blood donations from Magen David Adom, Israel or from Sheba Medical Center Blood Bank Laboratories, Israel; IRB - 1634-1). The studies reported in the manuscript abide by the Declaration of Helsinki principles.

Pf-iRBCs were incubated at 37 °C in a gas mixture of 1% O_2 and 5% CO_2 in N_2. Parasites were maintained in RPMI medium pH 7.4 (Diagnovum, Cat# D840-P10), supplemented with 25 mg/ml 4-(2-hydroxyethyl)-1-piperazineethanesulfonic acid (Sigma Cat# H3375), 50 µg/ml hypoxanthine (Sigma, Cat# 4010CBC), 2 mg/ml sodium bicarbonate (J.T. Baker, Cat# 0263.1000), 20 lg/ml gentamycin (Sigma, Cat# G9654), and 0.5% Albumax II (Gibco, Cat# 11021045). Parasite growth was monitored using methanol-fixed Giemsa-stained blood smears. *Pf*-infected RBC cultures were tested for *Mycoplasma* once a month using a commercial kit, MycoAlert Plus (Lonza, Cat# LT07-318).

Isolation of EVs

EVs were isolated from Ui RBCs or from *Pf*-iRBCs with high parasitemia levels (5% - 10% parasitemia) by collecting cell-free growth culture media (200 ml from Ui or *Pf*-iRBCs) and using the differential centrifugation method as reported previously (29). Briefly, cells were removed at subsequent centrifugations at 413*g*, 1900*g*, and 15,180*g*. The obtained supernatants (∼200 ml) were filtered through a 0.45 µm pore filter (Thermo Fisher Scientific Cat# 166-0045) and then concentrated using Vivacell units with molecular weight cut-off of 100 kDa (Sartorius AG, Cat# VC1042), following manufacturer instructions. Then, the EVs were pelleted by ultracentrifugation at 150,000*g* for 16 h at 4 °C. The pellet was carefully resuspended in sterile Ca^{2+}- and Mg^{2+}-free PBS (PBS −/−, Sartorius, Cat# 02-023-1A) for further analysis.

Nanoparticle tracking analysis

Vesicle size distribution and concentration were calculated using NTA (48) with the NanoSight NS300 device (Malvern Panalytical Ltd. Instruments) using a 405 nm or 488 nm filter. Sample size distributions were calibrated in a liquid suspension by the analysis of Brownian motion *via* light scattering, and the size of the particles was estimated based on their hydrodynamic radius (48).

EV purification using sucrose cushion

Resuspended EVs were loaded over a 20% sucrose solution gradient (29). EVs were pelleted by ultracentrifugation using a swinging bucket rotor (Beckman Coulter) at 100,000*g* for 4 h.

The pelleted EVs were resuspended in sterile PBS −/− for further analyses.

Atomic force microscopy

A freshly cleaved mica surface was incubated with 10 mM $MgCl_2$ solution for 1 min and then rinsed with PBS−/−. *Pf* EVs were placed on the Mg-modified mica and prior to scanning, PBS (Ca^{2+} -/Mg^{2+}) was added to the sample, followed by washing procedure performed carefully to avoid passing the interface. AFM imaging was performed on a JPK Nanowizard III AFM microscope (Bruker Nano GmbH) in QI mode. Measurements were conducted with a qp-BioAC-CI probe (Nanosensors), spring constant 0.06 N/m. Detector sensitivity and spring constant were determined using the JPK software. Image analysis was performed using Gwyddion (88) (version 2.65) or JPK-SPM data processing software (version 6.2.172).

Density gradient ultracentrifugation

EVs were fractionated through a 5%, 10%, 20%, and 40% OptiPrep (Axis-Shield, Cat# AXS-1114542) discontinuous gradient and ultracentrifugation (100,000*g*, 18 h, 4 °C) using a swinging rotor (Beckman Coulter). One milliliter fractions were collected from the top of the gradient for further analysis. EV fractions (fractions 6, 7, 8) were pooled, diluted with PBS−/−, and concentrated by an additional 4 h ultracentrifugation. The fractions were chosen based on the presence of EVs as verified by NTA. The EV pellet was resuspended in PBS −/− and subjected for cryo-TEM analysis.

Preparation of cryo-TEM samples

Cryo-TEM samples of EVs were prepared on either lacey carbon or C−flat EM grids (Electron Microscopy Sciences), on which 10 nm Protein A colloidal gold particles (Au − NP) were pre-adsorbed (Aurion). Au−NP adsorbed grids were then glow-discharged (30 s, 25 mA) in a Pelco EasiGlow system. An aliquot of the aqueous solution of the sample was applied on to the carbon side of EM grids, which was then incubated in the humidity chamber of the instrument at 100% humidity and room temperature and subsequently blotted for 4.0 s at blot force −10 and plunge-frozen into the precooled liquid ethane with a Vitrobot Mark IV (FEI).

Cryo-transmission electron microscopy

Cryo-electron micrographs of vitrified samples were collected using a transmission electron microscope Talos Arctica G3 TEM/STEM (Thermo Fisher Scientific), equipped with a OneView camera (Gatan) at accelerating voltage of 200 kV. Grid mapping and image acquisition were performed using SerialEM software (89) at a nominal magnification of 180x and 13500x, respectively. High magnification images were recorded at 73000x nominal magnification (0.411 nm pixel size) with a −3.5 µm defocus value. To minimize radiation damage during image acquisition, low-dose mode in SerialEM software was used and electron dose was kept below 100 e− Å − 2. Size quantification of recorded EV micrographs was performed with Fiji (ImageJ) (90, 91) by measuring the area covered by each vesicle and extrapolating the corresponding diameter. For each fraction, three separate biological replicates were plunge-frozen and visualized *via* cryo-TEM on separate days.

EV membrane staining

EV pellets derived from Ui RBCs and *Pf*-iRBCs samples were resuspended in PBS−/− and were labeled for DNA using DRAQ5 nucleic dye (excitation/emission 633/695 nm; 1, 5-bis {[2-(di-methylamino)ethyl]amino}-4, 8-dihydroxyanthracene-9, 10-dione; Abcam, Cat# 108410) by incubation at the final concentration of 1:500 vol/vol, 20 min at 37 °C. DNA labeling was followed by staining with lipophilic membrane R18 dye (Rhodamine B octadecyl ester perchlorate (Sigma, Cat# 83685), with excitation/emission 556/578 nm). The R18 stock of 2 mg/ml in DMSO was stored at −20 °C. R18 was used at the final concentration 1:500 vol/vol (58); with incubation at 37 °C for 20 min. Alternative lipid dye used to label EV membrane lipid components was ExoBrite 560/585 CTB EV Staining probe (562/584 nm; Cat# 30113-T; stored at 4oC; Biotium). Original ExoBrite 560 staining protocol provided by the manufacturer was modified to diminish the presence of free dye molecules. Briefly, the EV samples were stained at the concentration of 1:100 and incubated in 37 °C for 30 min. Unstained and stained EV samples were loaded on 20% sucrose cushion and ultracentrifuged as described before (29). The obtained pellets were resuspended in 150 µl of PBS−/−. The nanoparticle concentration was measured using NTA (NS300 NanoSight). At the end of experiments, EVs were treated with a TRITON X-100 detergent (Sigma, Cat# X100-500 ml) at the final concentration of 0.2 to 0.4% at RT for 30 min (68).

Spectral flow cytometry analysis

EV samples were subjected for spectral flow cytometry analysis using a 5 laser Cytek Aurora spectral flow cytometer (Cytek Biosciences). The gains of FSC and SSC (collected from the violet laser) detectors were set to 509 and 161, respectively. The detection threshold used for EV-R18 and EV-ExoBrite 560 was set at yellow green 1 (YG1, wavelength 567−587 nm) detector channel at gain of 500, the peak channel of both membrane dyes. DRAQ5-single stained samples were collected while the threshold was set at red 3 (R3, 683−707 nm) detector gain of 500. The gains of all the fluorescence detectors were enhanced equally by 225% compared to default Cytek Assay Settings to increase their sensitivity to weak signals but, at the same time, to maintain detection of the unique spectral signature of fluorescent dyes. Specifically, for YG1 and R3 detectors, the gains were set to 829 and 920, respectively.

Unstained and fluorescently labeled EV samples of equal volumes of 40 µl were collected at low acquisition mode of 15 µl/min (to minimize/exclude swarm effect). The final EV concentrations are presented as number of particles per ml and refer to the working dilutions of the cushion-purified EV samples (1:6 or 1:12 dilutions in PBS−/−). The data acquisition,

autofluorescence deduction, and spectral unmixing have been performed using SpectroFlo Software v3.3.0.

Statistical analysis

The bar plots and statistical analyses were carried out using GraphPad Prism v10.2.0 software. The comparisons of independent samples (*i.e.*, Ui and *Pf* EVs) were performed using two-tailed unpaired Student's t tests. The comparisons of dependent samples were performed using two-tailed paired Student's t tests. Specifically, paired Student's *t* test was applied to compare *Pf* EVs concentrations of ring and trophozoite stage *Pf* EVs, as well as for concentration of *Pf* EVs before and after detergent treatment. The data are presented as means ± SEM of EV concentrations/ml, referring to working dilutions of EV samples (post labeling and Cushion purification). The numbers of biological replicates (n) are provided in the legends to the figures. $p \leq 0.05$ was considered significant.

Graphic schemes of unstained and stained EVs were prepared using *BioRender.com*. The illustrations were prepared using *Adobe Illustrator* v28.4.1.

Data availability

The datasets generated during the current study are available in the public repository Zenodo: https://doi.org/10.5281/zenodo.15005218.

Supporting information—This article contains supporting information.

Acknowledgments—We would like to thank Dr Ziv Porat, the head of the Flow Cytometry Unit of the Weizmann Institute of Science, for his valuable comments. We would like to thank Dr Tally Rosenberg from the Flow Cytometry Unit of the Weizmann Institute of Science for assistance with the spectral flow cytometry instrument.
Views and opinions expressed are, however, those of the author(s) only and do not necessarily reflect those of the European Union or the European Research Council. Neither the European Union nor the granting authority can be held responsible for them. N. R. R. is deeply grateful for the support of the Henry Chanoch Krenter Institute for Biomedical Imaging and Genomics, the Dr Barry Sherman Institute for Medicinal Chemistry, the Karen Siem Fellowship for Women in Science, the Henri Gutwirth Award, and the Brenden-Mann Women's Innovation Impact Fund.

Author contributions—E. K., E. P.-K., R. R., and N. R.-R. writing–review and editing; E. K. and N. R.-R. writing–original draft; E. K. visualization; E. K. validation; E. K., E. P.-K., M. I. M., I. R.-G., and R. R. methodology; E. K., E. P.-K., Y. B., A. C. C., Y. S., M. I. M., and I. R.-G. investigation; E. K. formal analysis; E. K., M. I. M., I. R.-G., and R. R. data curation; E. K. conceptualization; N. R.-R. supervision.

Funding and additional information—N. R. R. is funded by the European Union (ERC, MalChemAtlas, 101086598). N. R. R. is supported by the Minerva Program support (grant number 714142), by the Israel Science Foundation (ISF) (grant No.1637/20), within the Israel Precision Medicine Partnership (IPMP) program and the Israel Science Foundation (ISF; Grant Application no.570/21) and Israel Science Foundation (ISF) - Canada-Israel Joint Health Research Program (IDRC, CIHR, and the Azrieli Foundation) Ref. number (P141807).

Conflict of interest—The authors declare that they have no conflicts of interests with the contents of this article.

Abbreviations—The abbreviations used are: AFM, atomic force microscopy; cryo-TEM, cryo-transmission electron microscopy; CTB, cholera toxin subunit B; EV, extracellular vesicle; FSC, forward scatter; MESF, Molecules of Equivalent Soluble Fluorophore; NTA, nanoparticle tracking analysis; *Pf*, *Plasmodium falciparum*; *Pf*-iRBCs; *Pf*-infectedRBCs; RBC, red blood cell; SSC, side scatter; Ui RBC, uninfected RBCs; Ui, uninfected.

References

1. Buzas, E. I. (2023) The roles of extracellular vesicles in the immune system. *Nat. Rev. Immunol.* **23**, 236–250
2. Sánchez-López, C. M., Trelis, M., Bernal, D., and Marcilla, A. (2021) Overview of the interaction of helminth extracellular vesicles with the host and their potential functions and biological applications. *Mol. Immunol.* **134**, 228–235
3. Gill, S., Catchpole, R., and Forterre, P. (2019) Extracellular membrane vesicles in the three domains of life and beyond. *FEMS Microbiol. Rev.* **042**, 273–303
4. Barillas-Mury, C., Ribeiro, J. M. C., and Valenzuela, J. G. (2022) Understanding pathogen survival and transmission by arthropod vectors to prevent human disease. *Science (1979)* **377**, eabc2757
5. Cai, Q., Halilovic, L., Shi, T., Chen, A., He, B., Wu, H., *et al.* (2023) Extracellular vesicles: cross-organismal RNA trafficking in plants, microbes, and mammalian cells. *Extracell Vesicles Circ. Nucl. Acids* **4**, 262–282
6. Ofir-Birin, Y., Heidenreich, M., and Regev-Rudzki, N. (2017) Pathogen-derived extracellular vesicles coordinate social behaviour and host manipulation. *Semin. Cell Dev. Biol.* **67**, 83–90
7. Buck, A. H., Coakley, G., Simbari, F., McSorley, H. J., Quintana, J. F., Le Bihan, T., *et al.* (2014) Exosomes secreted by nematode parasites transfer small RNAs to mammalian cells and modulate innate immunity. *Nat. Commun.* **5**, 5488
8. Chow, F. W.-N., Koutsovoulos, G., Ovando-Vázquez, C., Neophytou, K., Bermúdez-Barrientos, J. R., Laetsch, D. R., *et al.* (2019) Secretion of an Argonaute protein by a parasitic nematode and the evolution of its siRNA guides. *Nucleic Acids Res.* **47**, 3594–3606
9. Cruz Camacho, A., Alfandari, D., Kozela, E., and Regev-Rudzki, N. (2023) Biogenesis of extracellular vesicles in protozoan parasites: the ESCRT complex in the trafficking fast lane? *PLoS Pathog.* **19**, e1011140
10. Olajide, J. S., and Cai, J. (2020) Perils and promises of pathogenic Protozoan extracellular vesicles. *Front. Cell Infect. Microbiol.* **10**, 371
11. Sánchez-López, C. M., González-Arce, A., Ramírez-Toledo, V., Bernal, D., and Marcilla, A. (2024) Unraveling new players in helminth pathology: extracellular vesicles from Fasciola hepatica and Dicrocoelium dendriticum exert different effects on hepatic stellate cells and hepatocytes. *Int. J. Parasitol.* **54**, 617–634
12. da Silva Lira Filho, A., Lafleur, A., Marcet-Palacios, M., and Olivier, M. (2024) Identification of potential novel proteomic markers of Leishmania spp.-derived exosomes. *Front. Cell Infect. Microbiol.* **14**, 1354636
13. Szempruch, A. J., Dennison, L., Kieft, R., Harrington, J. M., and Hajduk, S. L. (2016) Sending a message: extracellular vesicles of pathogenic protozoan parasites. *Nat. Rev. Microbiol.* **14**, 669–675
14. Tandoh, K. Z., Ibarra-Meneses, A. V., Langlais, D., Olivier, M., Torrecilhas, A. C., Fernandez-Prada, C., *et al.* (2024) Extracellular vesicles: translational agenda questions for three Protozoan parasites. *Traffic* **25**, e12935
15. Toda, H., Diaz-Varela, M., Segui-Barber, J., Roobsoong, W., Baro, B., Garcia-Silva, S., *et al.* (2020) Plasma-derived extracellular vesicles from

Plasmodium vivax patients signal spleen fibroblasts via NF-kB facilitating parasite cytoadherence. *Nat. Commun.* **11**, 2761
16. Ofir-Birin, Y., and Regev-Rudzki, N. (2019) Extracellular vesicles in parasite survival. *Science (1979)* **363**, 817–818
17. Alfandari, D., Cadury, S., Morandi, M. I., and Regev-Rudzki, N. (2023) Transforming parasites into their own foes: parasitic extracellular vesicles as a vaccine platform. *Trends Parasitol.* **39**, 913–928
18. Heaton, P. M. (2020) Challenges of developing novel vaccines with particular global health importance. *Front. Immunol.* **11**, 517290
19. Fuhrmann, G., Neuer, A. L., and Herrmann, I. K. (2017) Extracellular vesicles – a promising avenue for the detection and treatment of infectious diseases? *Eur. J. Pharmaceutics Biopharmaceutics* **118**, 56–61
20. Barnadas-Carceller, B., del Portillo, H. A., and Fernandez-Becerra, C. (2024) Extracellular vesicles as biomarkers in parasitic disease diagnosis. *Curr. Top Membr.* **94**, 187–223
21. Razim, A., Zabłocka, A., Schmid, A., Thaler, M., Černý, V., Weinmayer, T., *et al.* (2024) Bacterial extracellular vesicles as intranasal postbiotics: detailed characterization and interaction with airway cells. *J. Extracell Vesicles* **13**, e70004
22. Huang, G., Lin, G., Zhu, Y., Duan, W., and Jin, D. (2020) Emerging technologies for profiling extracellular vesicle heterogeneity. *Lab. Chip* **20**, 2423–2437
23. Erdbrügger, U., and Lannigan, J. (2016) Analytical challenges of extracellular vesicle detection: a comparison of different techniques. *Cytometry A* **89**, 123–134
24. Bordanaba-Florit, G., Royo, F., Kruglik, S. G., and Falcón-Pérez, J. M. (2021) Using single-vesicle technologies to unravel the heterogeneity of extracellular vesicles. *Nat. Protoc.* **16**, 3163–3185
25. Cowman, A. F., Healer, J., Marapana, D., and Marsh, K. (2016) Malaria: biology and disease. *Cell* **167**, 610–624
26. Cox, F. E. (2010) History of the discovery of the malaria parasites and their vectors. *Parasit Vectors* **3**, 5
27. Brejt, J. A., and Golightly, L. M. (2019) Severe malaria. *Curr. Opin. Infect. Dis.* **32**, 413–418
28. Acharya, P., Garg, M., Kumar, P., Munjal, A., and Raja, K. D. (2017) Host–parasite interactions in human malaria: clinical implications of basic research. *Front. Microbiol.* **8**, 889
29. Abou Karam, P., Rosenhek-Goldian, I., Ziv, T., Ben Ami Pilo, H., Azuri, I., Rivkin, A., *et al.* (2022) Malaria parasites release vesicle subpopulations with signatures of different destinations. *EMBO Rep.* **23**, e54755
30. Ben Ami Pilo, H., Khan Khilji, S., Lühle, J., Biskup, K., Levy Gal, B., Rosenhek Goldian, I., *et al.* (2022) Sialylated *N* -glycans mediate monocyte uptake of extracellular vesicles secreted from *Plasmodium falciparum* -infected red blood cells. *J. Extracellular Biol.* **1**, e33
31. Dekel, E., Yaffe, D., Rosenhek-Goldian, I., Ben-Nissan, G., Ofir-Birin, Y., Morandi, M. I., *et al.* (2021) 20S proteasomes secreted by the malaria parasite promote its growth. *Nat. Commun.* **12**, 1172
32. Demarta-Gatsi, C., Rivkin, A., Di Bartolo, V., Peronet, R., Ding, S., Commere, P., *et al.* (2019) Histamine releasing factor and elongation factor 1 alpha secreted via malaria parasites extracellular vesicles promote immune evasion by inhibiting specific T cell responses. *Cell Microbiol.* **21**, e13021
33. Kioko, M., Pance, A., Mwangi, S., Goulding, D., Kemp, A., Rono, M., *et al.* (2023) Extracellular vesicles could be a putative posttranscriptional regulatory mechanism that shapes intracellular RNA levels in Plasmodium falciparum. *Nat. Commun.* **14**, 6447
34. Mantel, P.-Y., Hjelmqvist, D., Walch, M., Kharoubi-Hess, S., Nilsson, S., Ravel, D., *et al.* (2016) Infected erythrocyte-derived extracellular vesicles alter vascular function via regulatory Ago2-miRNA complexes in malaria. *Nat. Commun.* **7**, 12727
35. Regev-Rudzki, N., Wilson, D. W., Carvalho, T. G., Sisquella, X., Coleman, B. M., Rug, M., *et al.* (2013) Cell-cell communication between malaria-infected red blood cells via exosome-like vesicles. *Cell* **153**, 1120–1133
36. Ofir-Birin, Y., Abou Karam, P., Rudik, A., Giladi, T., Porat, Z., and Regev-Rudzki, N. (2018) Monitoring extracellular vesicle cargo active uptake by imaging flow cytometry. *Front. Immunol.* **9**, 1011
37. Ofir-Birin, Y., Ben Ami Pilo, H., Cruz Camacho, A., Rudik, A., Rivkin, A., Revach, O.-Y., *et al.* (2021) Malaria parasites both repress host CXCL10 and use it as a cue for growth acceleration. *Nat. Commun.* **12**, 4851
38. Alfandari, D., Ben Ami Pilo, H., Abou Karam, P., Dagan, O., Joubran, C., Rotkopf, R., *et al.* (2022) Monitoring distribution dynamics of EV RNA cargo within recipient monocytes and macrophages. *Front. Cell Infect. Microbiol.* **11**, 739628
39. Ye, W., Chew, M., Hou, J., Lai, F., Leopold, S. J., Loo, H. L., *et al.* (2018) Microvesicles from malaria-infected red blood cells activate natural killer cells via MDA5 pathway. *PLoS Pathog.* **14**, e1007298
40. Sisquella, X., Ofir-Birin, Y., Pimentel, M. A., Cheng, L., Abou Karam, P., Sampaio, N. G., *et al.* (2017) Malaria parasite DNA-harbouring vesicles activate cytosolic immune sensors. *Nat. Commun.* **8**, 1985
41. Combes, V., Taylor, T. E., Juhan-Vague, I., Mège, J.-L., Mwenechanya, J., Tembo, M., *et al.* (2004) Circulating endothelial microparticles in Malawian children with severe falciparum malaria complicated with coma. *JAMA: J. Am. Med. Assoc.* **291**, 2542–2544
42. Couper, K. N., Barnes, T., Hafalla, J. C. R., Combes, V., Ryffel, B., Secher, T., *et al.* (2010) Parasite-derived plasma microparticles contribute significantly to malaria infection-induced inflammation through potent macrophage stimulation. *PLoS Pathog.* **6**, e1000744
43. Pankoui Mfonkeu, J. B., Gouado, I., Fotso Kuaté, H., Zambou, O., Combes, V., Raymond Grau, G. E., *et al.* (2010) Biochemical markers of nutritional status and childhood malaria severity in Cameroon. *Br. J. Nutr.* **104**, 886–892
44. Nantakomol, D., Dondorp, A. M., Krudsood, S., Udomsangpetch, R., Pattanapanyasat, K., Combes, V., *et al.* (2011) Circulating red cell–derived microparticles in human malaria. *J. Infect. Dis.* **203**, 700–706
45. Kowal, J., Arras, G., Colombo, M., Jouve, M., Morath, J. P., Primdal-Bengtson, B., *et al.* (2016) Proteomic comparison defines novel markers to characterize heterogeneous populations of extracellular vesicle subtypes. *Proc. Natl. Acad. Sci. U. S. A.* **113**, E968–E977
46. Tkach, M., Kowal, J., and Théry, C. (2018) Why the need and how to approach the functional diversity of extracellular vesicles. *Philosophical Trans. R. Soc. B: Biol. Sci.* **373**, 20160479
47. Zhang, H., Freitas, D., Kim, H. S., Fabijanic, K., Li, Z., Chen, H., *et al.* (2018) Identification of distinct nanoparticles and subsets of extracellular vesicles by asymmetric flow field-flow fractionation. *Nat. Cell Biol.* **20**, 332–343
48. Filipe, V., Hawe, A., and Jiskoot, W. (2010) Critical evaluation of nanoparticle tracking analysis (NTA) by NanoSight for the measurement of nanoparticles and protein aggregates. *Pharm. Res.* **27**, 796–810
49. Gardiner, C., Vizio, D. Di, Sahoo, S., Théry, C., Witwer, K. W., Wauben, M., *et al.* (2016) Techniques used for the isolation and characterization of extracellular vesicles: results of a worldwide survey. *J. Extracell Vesicles* **5**, 32945
50. Rosenhek-Goldian, I., Abou Karam, P., Regev-Rudzki, N., and Rojas, A. (2022) Imaging of extracellular vesicles derived from Plasmodium falciparum-infected red blood cells using atomic force microscopy. *Methods Mol. Biol.* **2470**, 133–145
51. Morandi, M. I., Busko, P., Ozer-Partuk, E., Khan, S., Zarfati, G., Elbaz-Alon, Y., *et al.* (2022) Extracellular vesicle fusion visualized by cryo-electron microscopy. *PNAS Nexus* **1**, pgac156
52. Kozela, E., Meneghetti, P., Regev-Rudzki, N., Torrecilhas, A. C., and Porat, Z. (2024) Subcellular particles for characterization of host-parasite interactions. *Microbes Infect.* **26**, 105314
53. Dekel, E., Abou Karam, P., Ohana-Daniel, Y., Biton, M., Regev-Rudzki, N., and Porat, Z. (2020) Antibody-free labeling of malaria-derived extracellular vesicles using flow cytometry. *Biomedicines* **8**, 98
54. Nolan, J. P. (2022) The evolution of spectral flow cytometry. *Cytometry Part A* **101**, 812–817
55. Nolan, J. P., and Condello, D. (2013) Spectral flow cytometry. *Curr. Protoc. Cytom* **1**, 1.27.1–1.27.13
56. Welsh, J. A., A Arkesteijn, G. J., Bremer, M., Cimorelli, M., Dignat-George, F., Giebel, B., *et al.* (2023) A compendium of single extracellular vesicle flow cytometry. *J. Extracell Vesicles* **12**, 12299
57. Théry, C., Witwer, K. W., Aikawa, E., Alcaraz, M. J., Anderson, J. D., Andriantsitohaina, R., *et al.* (2018) Minimal information for studies of

extracellular vesicles 2018 (MISEV2018): a position statement of the International Society for Extracellular Vesicles and update of the MISEV2014 guidelines. *J. Extracell Vesicles* **7**, 1535750
58. Chuo, S. T.-Y., Chien, J. C.-Y., and Lai, C. P.-K. (2018) Imaging extracellular vesicles: current and emerging methods. *J. Biomed. Sci.* **25**, 91
59. Hassdenteufel, S., and Schuldiner, M. (2022) Show your true color: mammalian cell surface staining for tracking cellular identity in multiplexing and beyond. *Curr. Opin. Chem. Biol.* **66**, 102102
60. Simonsen, J. B. (2017) What are we looking at? Extracellular vesicles, lipoproteins, or both? *Circ. Res.* **121**, 920–922
61. Botha, J., Handberg, A., and Simonsen, J. B. (2022) Lipid-based strategies used to identify extracellular vesicles in flow cytometry can be confounded by lipoproteins: evaluations of annexin V, lactadherin, and detergent lysis. *J. Extracell Vesicles* **11**, e12200
62. Buntsma, N. C., Shahsavari, M., Gąsecka, A., Nieuwland, R., van Leeuwen, T. G., and van der Pol, E. (2023) Preventing swarm detection in extracellular vesicle flow cytometry: a clinically applicable procedure. *Res. Pract. Thromb. Haemost.* **7**, 100171
63. Lai, R. C., and Lim, S. K. (2019) Membrane lipids define small extracellular vesicle subtypes secreted by mesenchymal stromal cells. *J. Lipid Res.* **60**, 318–322
64. Fantini, J. (2023) Lipid rafts and human diseases: why we need to target gangliosides. *FEBS Open Bio.* **13**, 1636–1650
65. Ben-Hur, S., Biton, M., and Regev-Rudzki, N. (2019) Extracellular vesicles: a prevalent tool for microbial gene delivery? *Proteomics* **19**, e1800170
66. Smith, P. J., Wiltshire, M., and Errington, R. J. (2004) DRAQ5 labeling of nuclear DNA in live and fixed cells. *Curr Protoc Cytom* **7**, 7.25
67. Clancy, J. W., Sheehan, C. S., Boomgarden, A. C., and D'Souza-Schorey, C. (2022) Recruitment of DNA to tumor-derived microvesicles. *Cell Rep.* **38**, 110443
68. Osteikoetxea, X., Sódar, B., Németh, A., Szabó-Taylor, K., Pálóczi, K., Vukman, K. V., *et al.* (2015) Differential detergent sensitivity of extracellular vesicle subpopulations. *Org. Biomol. Chem.* **13**, 9775–9782
69. Boudna, M., Campos, A. D., Vychytilova-Faltejskova, P., Machackova, T., Slaby, O., and Souckova, K. (2024) Strategies for labelling of exogenous and endogenous extracellular vesicles and their application for in vitro and in vivo functional studies. *Cell Commun. Signaling.* **22**, 171
70. Lai, C. P., Kim, E. Y., Badr, C. E., Weissleder, R., Mempel, T. R., Tannous, B. A., *et al.* (2015) Visualization and tracking of tumour extracellular vesicle delivery and RNA translation using multiplexed reporters. *Nat. Commun.* **6**, 7029
71. Adan, A., Alizada, G., Kiraz, Y., Baran, Y., and Nalbant, A. (2017) Flow cytometry: basic principles and applications. *Crit. Rev. Biotechnol.* **37**, 163–176
72. Gul, B., Syed, F., Khan, S., Iqbal, A., and Ahmad, I. (2022) Characterization of extracellular vesicles by flow cytometry: challenges and promises. *Micron.* **161**, 103341
73. Hendrix, A., Lippens, L., Pinheiro, C., Théry, C., Martin-Jaular, L., Lötvall, J., *et al.* (2023) Extracellular vesicle analysis. *Nat. Rev. Methods Primers* **3**, 56
74. McKinnon, K. M. (2018) Flow cytometry: an overview. *Curr Protoc Immunol* **120**, 5.1.1–5.1.11
75. Morales-Kastresana, A., Telford, B., Musich, T. A., McKinnon, K., Clayborne, C., Braig, Z., *et al.* (2017) Labeling extracellular vesicles for nanoscale flow cytometry. *Sci. Rep.* **7**, 1878
76. Simeone, P., Celia, C., Bologna, G., Ercolino, E., Pierdomenico, L., Cilurzo, F., *et al.* (2020) Diameters and fluorescence calibration for extracellular vesicle analyses by flow cytometry. *Int. J. Mol. Sci.* **21**, 7885
77. van der Vlist, E. J., Nolte-'t Hoen, E. N. M., Stoorvogel, W., Arkesteijn, G. J. A., and Wauben, M. H. M. (2012) Fluorescent labeling of nano-sized vesicles released by cells and subsequent quantitative and qualitative analysis by high-resolution flow cytometry. *Nat. Protoc.* **7**, 1311–1326
78. Kuiper, M., van de Nes, A., Nieuwland, R., Varga, Z., and van der Pol, E. (2021) Reliable measurements of extracellular vesicles by clinical flow cytometry. *Am. J. Reprod. Immunol.* **85**, e13350
79. van der Pol, E., Sturk, A., van Leeuwen, T., Nieuwland, R., Coumans, F., Mobarrez, F., *et al.* (2018) Standardization of extracellular vesicle measurements by flow cytometry through vesicle diameter approximation. *J. Thromb. Haemost.* **16**, 1236–1245
80. Woud, W. W., Pugsley, H. R., Bettin, B. A., Varga, Z., and van der Pol, E. (2024) Size and fluorescence calibrated imaging flow cytometry: from arbitrary to standard units. *Cytometry Part A* **105**, 752–762
81. de Rond, L., van der Pol, E., Bloemen, P. R., Van Den Broeck, T., Monheim, L., Nieuwland, R., *et al.* (2020) A systematic approach to improve scatter sensitivity of a flow cytometer for detection of extracellular vesicles. *Cytometry A* **97**, 582–591
82. van der Pol, E., Coumans, F. A. W., Grootemaat, A. E., Gardiner, C., Sargent, I. L., Harrison, P., *et al.* (2014) Particle size distribution of exosomes and microvesicles determined by transmission electron microscopy, flow cytometry, nanoparticle tracking analysis, and resistive pulse sensing. *J. Thromb Haemost.* **12**, 1182–1192
83. van der Pol, E., van Gemert, M. J. C., Sturk, A., Nieuwland, R., and van Leeuwen, T. G. (2012) Single vs. swarm detection of microparticles and exosomes by flow cytometry. *J. Thromb. Haemost.* **10**, 919–930
84. Aibaidula, A. Z., Fain, C. E., Garcia, L. C., Wier, A., Bouchal, S. M., Bauman, M. M., *et al.* (2023) Spectral flow cytometry identifies distinct nonneoplastic plasma extracellular vesicle phenotype in glioblastoma patients. *Neurooncol. Adv.* **5**, vdad082
85. Brandenburg, B., Koudstaal, W., Goudsmit, J., Klaren, V., Tang, C., Bujny, M. V., *et al.* (2013) Mechanisms of hemagglutinin targeted influenza virus neutralization. *PLoS One* **8**, e80034
86. Schwartz, A., Gaigalas, A. K., Wang, L., Marti, G. E., Vogt, R. F., and Fernandez-Repollet, E. (2004) Formalization of the MESF unit of fluorescence intensity. *Cytometry B Clin. Cytom.* **57B**, 1–6
87. Trager, W., and Jensen, J. B. (1976) Human malaria parasites in continuous culture. *Science (1979)* **193**, 673–675
88. Nečas, D., and Klapetek, P. (2012) Gwyddion: an open-source software for SPM data analysis. *Open Phys.* **10**, 181–188
89. Mastronarde, D. N. (2003) SerialEM: a program for automated tilt series acquisition on tecnai microscopes using prediction of specimen position. *Microsc. Microanalysis* **9**, 1182–1183
90. Rueden, C. T., Schindelin, J., Hiner, M. C., DeZonia, B. E., Walter, A. E., Arena, E. T., *et al.* (2017) ImageJ2: ImageJ for the next generation of scientific image data. *BMC Bioinformatics* **18**, 529
91. Schindelin, J., Arganda-Carreras, I., Frise, E., Kaynig, V., Longair, M., Pietzsch, T., *et al.* (2012) Fiji: an open-source platform for biological-image analysis. *Nat Methods* **9**, 676–682